K-shell photoionization of O^{+} and O^{2+} ions: Experiment and theory

J. M. Bizau, D. Cubaynes, S. Guilbaud, M. M. Al Shorman, M. F. Gharaibeh, I. Q. Ababneh, C. Blancard, and B. M. McLaughlin

Phys. Rev. A **92**, 023401 — Published 3 August 2015

DOI: 10.1103/PhysRevA.92.023401

K-Shell photoionization of O^+ and O^{2+} ions: experiment and theory

J M Bizau[1,2]*, D Cubaynes[1,2], S Guilbaud[1], M M Al Shorman[1]

[1]Institut des Sciences Moléculaires d'Orsay (ISMO), CNRS UMR 8214, Université Paris-Sud, Bât. 350, F-91405 Orsay cedex, France

[2]Synchrotron SOLEIL - L'Orme des Merisiers, Saint-Aubin - BP 48 91192 Gif-sur-Yvette cedex, France

M F Gharaibeh†

Department of Mathematics, Statistics and Physics, P.O.Box 2713, Qatar University, Doha, Qatar

I Q Ababneh

Department of Physics, Jordan University of Science and Technology, Irbid 22110, Jordan

C Blancard

CEA-DAM-DIF, Bruyères-le-Châtel, F-91297 Arpajon Cedex, France

B M McLaughlin*

Centre for Theoretical Atomic, Molecular and Optical Physics (CTAMOP), School of Mathematics and Physics, The David Bates Building, 7 College Park,
Queen's University Belfast, Belfast BT7 1NN, UK

Institute for Theoretical Atomic and Molecular Physics (ITAMP), Harvard Smithsonian Center for Astrophysics, MS-14, Cambridge, MA 02138, USA

Abstract. Absolute cross sections for the single and double K-shell photoionization of carbon-like O^{2+} and nitrogen-like O^+ ions were measured in the 526 eV to 620 eV photon energy range by employing the ion-photon merged-beam technique at the SOLEIL synchrotron radiation facility. High-resolution spectroscopy up to $E/\Delta E \approx 5300$ was achieved. Rich resonance structures observed in the experimental spectra are analyzed and identified with the aid of *R*-matrix and MCDF methods. For these two atomic oxygen ions of particular astrophysical interest we characterized the strong $1s \rightarrow 2p$ and the weaker $1s \rightarrow np$ ($n>2$) resonances observed for. A detailed comparison of the energies of the $1s \rightarrow 2p$ resonances in the first members of the oxygen iso-nuclear sequence measured by synchrotron based experiments and the Chandra and XMM-Newton X-ray satellites is presented.

PACS numbers: 32.80.Fb, 31.15.Ar, 32.80.Hd, and 32.70.-n

* Corresponding authors, E-mail: jean-marc.bizau@u-psud.fr, b.mclaughlin@qub.ac.uk

†Leave Address: Department of Physics, Jordan University of Science and Technology, Irbid 22110, Jordan

1. Introduction

Photoionization cross sections on multiply-charged ions are provided mainly by theoretical methods, and the test of their results by experiment stays an urgent task. In particular, a recent multiplication of theoretical studies on K-shell photoionization cross sections has been motivated by the observation from X-ray satellites, like *Chandra* and *XMM Newton*, of intense lines identified as K_α transitions in light elements and their ions. The high flux of X-ray radiation provided by the insertion devices in the third generation synchrotron radiation (SR) facilities allows now for an accurate experimental determination of the photoionization cross sections on multiply-charged ions. Oxygen is the third most abundant element in the Universe, after hydrogen and helium. K-shell photoabsorption of oxygen and its ions is often responsible for prominent features in the interstellar medium (ISM) absorption spectra in the 500 eV to 600 eV photon energy range. Indeed oxygen K-shell absorption lines have been observed towards both low-mass X-ray binaries [1-5] and active nucleus of Seyfert galaxies [6-8].

In the present investigation we present detailed measurements of the absolute K-shell single and double photoionization cross sections for O^+ and O^{2+} ions in the 530 eV - 620 eV photon energy region, using the merged-beam setup at SOLEIL SR facility. This work is a continuation of our previous study on the O^{3+} ion [9]. As the ions were produced in an electron cyclotron resonance ion source (ECRIS), both ions in their respective ground and metastable states contributed to the experimental spectra. In parallel, theoretical predictions are made using both the multi-configuration Dirac-Fock (MCDF) and the Breit-Pauli *R*-matrix (BPRM) with pseudo-states methods, to compare with the measurements and assist in the determination of the metastable content of the ion beams. These calculations enable the identification and characterization of the strong $1s \rightarrow 2p$ (K_α) and the weaker $1s \rightarrow np$, $n>2$ resonance peaks observed in both the C-like (O^{2+}) and the N-like (O^+) oxygen spectra. The present investigation provides absolute values (experimental and theoretical) for photoionization cross sections, resonance energies and resonance oscillator strengths and, for the $1s \rightarrow 2p$ transitions, natural line widths.

Prior to the present study, extensive photoionization cross section calculations were performed first in the single electron approximation [10,11], a method often giving a good description of the direct photoionization processes but completely ignoring the resonant

photoexcitations responsible for the strong absorption lines observed in the spectra. More recent works include electron correlation effects, and we will quote here only those related to O^+ or O^{2+} ions. Firstly, Chen and co-workers [12] have calculated K-shell Auger decay and radiative transitions in the carbon isoelectronic sequences using the MCDF approach. Calculations for Auger inner-shell processes subsequently used the *R*-matrix method [13-17]. García and co-workers [18] extended these works by using the BPRM with an optical potential method, to describe the Auger and radiation damping within an intermediate-coupling scheme. Photoionization from the ground state was investigated along the oxygen iso-nuclear sequence in the photon energy region of the K-edge. Their calculated cross sections were incorporated in the XSTAR modeling codes used to reconstruct the ISM absorption spectra [19,20].

Few experiments have been devoted to the study of K-shell excitation in oxygen ions. Auger spectra of singly and doubly core-excited oxygen ions emitted in the collision of fast oxygen-ion beams with gas targets and foils were measured by Bruch and co-workers [21]. K-shell X-ray lines from inner-shell excited O^{2+} to O^{5+} ions were observed using an electron beam ion trap (EBIT) [22]. The merged-beam technique was used at Spring-8 to measure, with a low resolving power ($E/\Delta E \approx 310$), relative K-shell resonant photoionization cross sections for O^+ ions in the photon energy range of the $1s \rightarrow 2p$ photoexcitations [23]. Recently, we published high resolution ($\approx$ 5000 resolving power) absolute measurements performed at SOLEIL of the photoionization cross section for the O^{3+} ion in the energy range of the $1s \rightarrow 2p$ and $1s \rightarrow 3p$ photoexcitations [9].

Recent studies have pointed out some marked discrepancies between the energy of the K_α lines determined by the X-ray satellites and laboratory experiments and calculations. Gatuzz and co-workers [24] compared the Chandra spectra of a low mass X-ray binary star with the results of modeling using the XSTAR code. They noted for O and O^+ a displacement of the $1s \rightarrow 2p$ calculated lines with respect to the Chandra observations. The K-shell photoionization cross section of the neutral oxygen atom measured by Stolte *et al* [25,26] at the Advanced Light Source (ALS) gives a position for this line almost 0.8 eV lower than the energy deduced from Chandra observations [24], a difference distinctly outside the quoted uncertainties of both measurements. Similar disagreement was found between our previous measurements at SOLEIL and the Chandra and XMM Newton observations for the O^{3+} ion [9]. We have taken special care in the present work of the energy calibration for the experimental spectra to verify

if such discrepancies exist also for O^+ and O^{2+} ions. A reliable determination of the positions of the lines is of particular importance since the oxygen lines are often used to calibrate the energy scales of the X-ray observatories spectra due to the high abundance of this element.

The layout of the paper is as follows: Section 2 briefly outlines the experimental setup and procedure used, including the description of the energy calibration procedure; Section 3 presents the theoretical works; Section 4 presents the results and a discussion based on the comparison of the experimental and theoretical data. Finally in section 5 conclusions are drawn from the present investigation.

2. Experiment

2.1 *Ion production*

The present measurements were made using the MAIA (Multi-Analysis Ion Apparatus) set-up permanently installed on branch A of the PLEIADES beam line [27,28] at SOLEIL. The set-up and the experimental procedure are the same as the ones described in our previous paper on the O^{3+} ion [9] and have already been detailed in [29]. Here we will only give a brief description of the set-up and procedure.

The oxygen ions are produced in a permanent magnet ECRIS. A 12.6 GHz radio wave is used to heat the plasma, at a power of a few Watts. The ions are extracted from the plasma by application of a 4 kV bias on the source. The ion beam is selected according to mass/charge ratio by a dipole magnet and merged with the photon beam in the 50 cm long interaction region. After interaction, the charges of the resulting ions are analyzed by a second dipole magnet. The parent ions are collected in a Faraday cup, and the ions, which have increased their charge by one or two units due to the interaction with the photons (photoions), are counted using channel plates.

2.2 *Experimental procedure*

The merged-beam set-up enables the determination of absolute photoionization cross sections. At a given photon energy, the cross sections σ are obtained from:

$$\sigma = \frac{Se^2\eta vq}{IJ\varepsilon\int_0^L \frac{dz}{\Delta x \Delta y F(z)}} \qquad (1)$$

Where S is the counting rate of photoions measured with the channel-plates. A chopper, placed at the exit of the photon beam line, enables subtraction from the photoion signal of the noise produced by collisional ionization processes, charge stripping on the collimator slits or autoionizing decay of metastable excited states produced in the ECRIS source. In (1), q is the charge of the target ions, v is the velocity of the ions in the interaction region determined from the potentials applied to the ECRIS source and the interaction region (see below) and I is the current produced by the photons incident on an AXUV100 IRD® photodiode. The efficiency η of the photodiode was calibrated at the Physikalisch-Technische Bundesanstalt (PTB) beam line at BESSY in Berlin. e is the charge of the electron and J is the current of incident ions as measured by the Faraday cup. ε is the efficiency of the microchannel plates determined by comparing the counting rate produced by a low intensity ion beam and the current induced by the same beam in the Faraday cup. $\Delta x \Delta y F(z)$ is an effective beam area (z is the propagation axis of the two beams), where F is a two dimensional form factor determined using three sets of xy scanners placed at each end and in the middle of the interaction region. The length L of the interaction region is fixed by applying a bias (typically +800V) on a 50 cm long tube used as interaction region, resulting in a different velocity for the photoions produced inside and outside the tube. Typical values of the parameters involved in equation (1), measured at a photon energy of 537.27 eV for O^{2+} ions, are given in Table 1. The accuracy of the measured cross-sections is determined by statistical fluctuations of the photoion and noise counting rates and a systematic contribution resulting from the measurement of the different parameters in equation (1). The latter is estimated to be ~ 15% and is dominated by the uncertainties in the determination of the photon flux and the form factor.

To record the single (double) photoionization spectra, the field in the second dipole magnet is adjusted to detect with the channel plates the photoions which have gained one (two) charge(s) while the photon energy is scanned. Two acquisition modes have been used. One, called absolute mode in the following, corresponds to measurements done with the voltage applied to the 50 cm long tube to define the interaction length L, allowing the determination of the cross section in absolute value. In the second mode, we will call relative mode, no voltage is applied on the interaction tube, providing higher counting rates since the whole interaction length of the photon and ion beams is used, allowing to determine with a better resolution relative cross sections. They are then normalized to the cross sections recorded in the absolute mode by keeping the same integrated area of the lines in both spectra.

Table 1. Typical values for the experimental parameters involved in evaluating the absolute cross section at a photon energy of 537.27 eV with 2700 resolving power for O^{2+} ion.

Signal, S	770 Hz
Noise	200 Hz
Velocity, v	$2.7\ 10^5$ m s^{-1}
Photon flux	$2.2\ 10^{12}$ s^{-1}
Ion current, J	500 nA
Detector efficiency, ε	0.49
Integrated form factor	$4\ 10^4$ m^{-1}

2.3 *Excitation source and energy calibration*

The photon beam is the monochromatized synchrotron radiation from the PLEIADES beam line [25,26]. In the photon energy range considered here, a permanent magnet Apple II undulator with 80 mm period is used. The light is monochromatized by a plane gratings monochromator with no entrance slit. The high-flux 600 lines/mm grating was used for this work. High spectral purity is obtained by the cut of the optics transmission and the use of gratings with varied groove depth.

The photon energy is determined using a double-ionization chamber of Samson type [30]. For this work, we used the 1s → 3*sσ* and 4*pσ* transitions in O_2 gas [31]. The main uncertainty in the photon energy determination results from the uncertainties, given in the literature, for the energies of the absorption lines used for calibration. To our knowledge, all the synchrotron radiation based experiments on the K-shell photoionization of O_2 refer to the electron energy loss spectroscopy (EELS) works of Brion and co-workers [32,33]. They determined the energy of the 1s → 1*π** transition at 530.8 eV with a stated accuracy of ±200 meV. By measuring the ion yield in a gas cell, Coreno and co-workers [34] improved the accuracy for this line to ±100 meV by normalization on the 1s → 1*π** transition EELS measurements, both for O_2 [33] and CO [35], the latter being quoted to an accuracy of ±90 meV. To double-check this determination independently of the relatively low-resolution

EELS measurements, we used a Scienta electron spectrometer installed on a second branch of the PLEIADES beam line. Firstly, the energy of the monochromator was fixed at the maximum of the 1s → 1π* O_2 line, using a gas cell present on the same branch. Then an electron spectrum of the Ne $2s^{-1}$ photoline was recorded. The kinetic energy (KE) scale of the electron spectrometer was calibrated by recording the O_2 Auger line at KE = 491.90±0.10 eV [36], a kinetic energy very close to the kinetic energy of the Ne $2s^{-1}$ photoline measured previously (482.65 eV). Taking the known binding energy of the Ne 2s subshell (48.475011 eV) from NIST tables [37], we determined an excitation energy of 530.70±0.15 eV for the center of the 1s → 1π* line, in agreement with the previous EELS (530.8±0.2 eV [38]) and ion yield (530.8±0.1 eV [34]) determinations, within their respective quoted uncertainties. The same procedure repeated at the maximum of the 1s → 3$s\sigma$ transition gave 539.17±0.15 eV, which is 0.22 eV higher than the energy given by Tanaka et al (538.95±0.04 eV) [31]. These two energy values do not overlap within their quoted uncertainties. However, the two determinations are compatible if we assume an uncertainty of ±100 meV for the energy given by Tanaka et al [31]. This value is more in accordance with the uncertainty given by Coreno et al [34] which is the reference quoted by Tanaka et al.

In the following, we use the energy we determined with the Scienta for the 1s → 3$s\sigma$ transition (539.17±0.15 eV) to calibrate the energy of the oxygen ion lines. An overall accuracy of ±180 meV for our energy determination was estimated as follows: 150 meV for the reference given by the Scienta, plus 30 meV to allow for the mechanical accuracy of the monochromator and the determination of the maxima of the lines in the ion yield spectra recorded with the gas cell. The photon energy was also corrected for the Doppler shift resulting from the velocity of the oxygen ions.

3. Theory

3.1 MCDF

Multi-configuration Dirac-Fock (MCDF) calculations were performed based on a full intermediate coupling regime in a jj-basis using the code developed by Bruneau [39]. Photoexcitation cross sections have been carried out for both C-like and N-like atomic oxygen ions in the region of the K-edge. Only electric dipole transitions have been computed using the length form. The photoexcitation cross sections involving 1s → np transitions have been considered for all the levels of the O^{2+} ion ground configuration, namely $1s^2\ 2s^2\ 2p^2\ {}^3P_{0,1,2}$,

$^1D_2$ and $^1S_0$. The metastable $1s^2\ 2s\ 2p^3\ ^5S_2$ level was also considered. Similarly photo-excitation cross sections involving 1s → np transitions have been considered for all the levels of the O^+ ion ground configuration, namely $1s^2\ 2s^2\ 2p^3\ ^4S_{3/2}$, $^2D_{3/2;5/2}$ and $^2P_{1/2,3/2}$.

For the C-like atomic oxygen ion the following initial configurations were considered: $1s^2\ 2s^2\ 2p^2$, $1s^2\ 2s^2\ 3l^2$ (l=s,p,d), $1s^2\ 2p^4$, $1s^2\ 2p^2\ 3l^2$ (l=s,p,d), and $1s^2\ 2s\ 2p^2\ n$p (n=2,…,6). The following final configurations were considered: $1s\ 2s^2\ 2p^2\ n$p and $1s\ 2s\ 2p^3\ n$p (n=2,…,6). In order to describe relaxation effects, radial functions with principal quantum number n=1 or 2 are not the same for initial and final configurations. Photoionization cross sections from the $1s^2\ 2s^2\ 2p^2$ and $1s^2\ 2s\ 2p^3$ configurations were calculated separately. For the N-like atomic oxygen ion the following initial configurations were considered: $1s^2\ 2s^2\ 2p^2\ n$p (n=2,…,5), $1s^2\ 2s^2\ 2p\ 3l^2$ (l=s,p,d), and $1s^2\ 2p^5$. The following final configurations were considered: $1s\ 2s^2\ 2p^3\ n$p and $1s\ 2p^5\ n$p (n=2,…,5). In order to describe relaxation effects, radial functions with principal quantum number n=1 or 2 are not the same for initial and final configurations. Photoionization cross sections from the $1s^2\ 2s^2\ 2p^3$ has been calculated separately.

3.2 R-matrix

The *R*-matrix method [40], with an efficient parallel implementation of the codes [41-43] was used to determine all the cross sections presented here, for both the initial $1s^22s^22p^2\ ^3P$ ground state and the excited $1s^22s^22p^2\ ^1D$, $1s^22s^22p^2\ ^1S$ and $1s^22s2p^3\ ^5S^o$ metastable states. Cross section calculations were carried out in LS- coupling with 390-levels retained in the close-coupling expansion. The Hartree-Fock 1s, 2s and 2p tabulated orbitals of Clementi and Roetti [44] were used with n=2 physical and n=3 pseudo orbitals of the O^{3+} ion determined by energy optimization on the appropriate physical and hole-shell states [45], using the atomic structure code CIV3 [46]. The n=3 pseudo-orbitals are included to account for core relaxation and additional correlation effects in the multi-configuration interaction wave functions. All the O^{3+} residual ion states were then represented by using multi-reference-configuration-interaction (MRCI) wave functions. The non-relativistic R-matrix approach was used to calculate the energies of the O^{2+} bound states and the subsequent photoionization cross sections. Photoionization cross sections out of the $1s^22s^22p^2\ ^3P$ ground state, the $1s^22s^22p^2\ ^1D$, $1s^22s^22p^2\ ^1S$ and the $1s^22s2p^3\ ^5S^o$ metastable states were then obtained for all total angular momentum scattering symmetries that contribute.

For N-like atomic oxygen both in the initial $1s^2 2s^2 2p^3\ ^4S^o$ ground state and the $1s^2 2s^2 2p^3\ ^2D^o, ^2P^o$ metastable states, the *R*-matrix method [40] was used to obtain all the cross section calculations in LS-coupling with 390-levels retained in the close-coupling expansion. The Hartree-Fock 1s, 2s and 2p tabulated orbitals of Clementi and Roetti [44] were used with n=2 physical and n=3 pseudo orbitals of the O^{2+} ion determined by energy optimization on the appropriate physical and hole-shell states [45], using the atomic structure code CIV3 [46]. The n=3 pseudo-orbitals are included to account for core relaxation and additional correlation effects in the multi-configuration interaction wave functions. All the O^{2+} residual ion states were then represented by using MRCI wave functions. The non-relativistic R-matrix approach was used to calculate the energies of the O^+ bound states and the subsequent photoionization cross sections. Photoionization cross sections out of the$1s^2 2s^2 2p^3\ ^4S^o$ ground state and the $1s^2 2s^2 2p^3\ ^2D^o$ and $1s^2 2s^2 2p^3\ ^2P^o$ metastable states were then obtained for all total angular momentum scattering symmetries that contribute.

3.3. Scattering

The current state-of-the-art parallel *R*-matrix codes running on high performance computers (HPC) world-wide, allows one to concurrently form and diagonalize large scale Hamiltonian and dipole matrices [47,48] required for electron or photon collisions with atomic systems allowing large-scale calculations to be completed in a timely manner. In the present *R*-matrix with pseudo-states (RMPS) calculations, for each ion, the scattering wave functions were generated by allowing three-electron promotions out of selected base configurations into the orbital set employed. Scattering calculations were performed with twenty continuum functions for each ion studied. For both of the ions for the ground state and the excited metastable states, the outer region electron-ion collision problem was solved (in the resonance region below and between all the thresholds) using a suitably chosen fine energy mesh of 2×10^{-7} Rydbergs (≈ 2.72 μeV) to fully resolve all the resonance structure in the photoionization cross sections. The peaks found in the theoretical photoionization cross section spectrum were fitted to Fano profiles for overlapping resonances [38,49,50] as opposed to the energy derivative of the eigenphase sum method [51-53].

4. Results and discussion

4.1 N-like O^+ ion

Photoionization cross sections were measured with different band passes (BP = 350 meV, 200 meV and 100 meV) in the region of the 1s → 2p resonances. Figure 1 displays the single photoionization cross section (detection of O^{2+} photoions) obtained with 200 meV (upper panel) and 100 meV BP (middle panel), as well as the double ionization cross section (detection of O^{3+} photoions) recorded with 200 meV BP (lower panel). The spectrum in the middle panel was obtained in the relative mode, and then normalized to absolute values using the spectrum (shown in the upper panel) recorded in the absolute mode. The double photoionization cross section was recorded in both relative (vertical bars) and absolute (open points) modes. For all cross sections, the vertical bars on each point represent the statistical uncertainties.

Photoexcitation of a 1s electron of the O^+ ion in the $1s^2\ 2s^2\ 2p^3\ ^4S°$ ground term can be represented by:

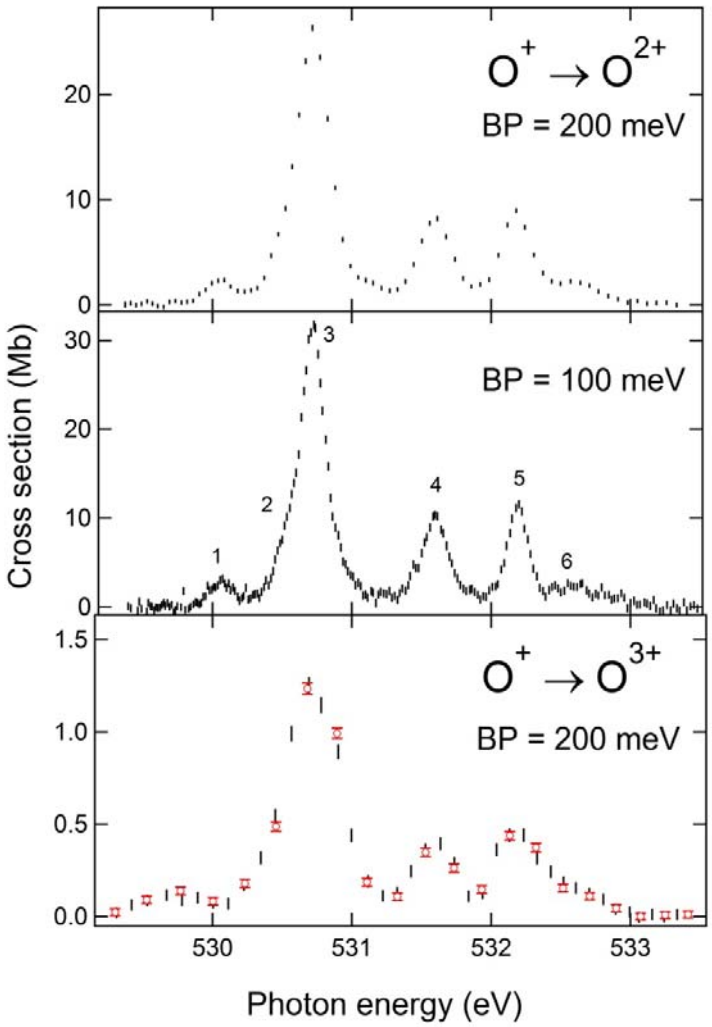

Figure 1. (color on line) Upper panel: Single photoionization cross section recorded in the absolute mode with 200 meV BP; Middle panel: Single photoionization cross section recorded in the relative mode with 100 meV BP; Lower panel: Double photoionization cross section recorded in the relative (vertical bars) and absolute (red open circles) modes with 200 meV BP. On all figures, the vertical bars indicate the statistical uncertainties.

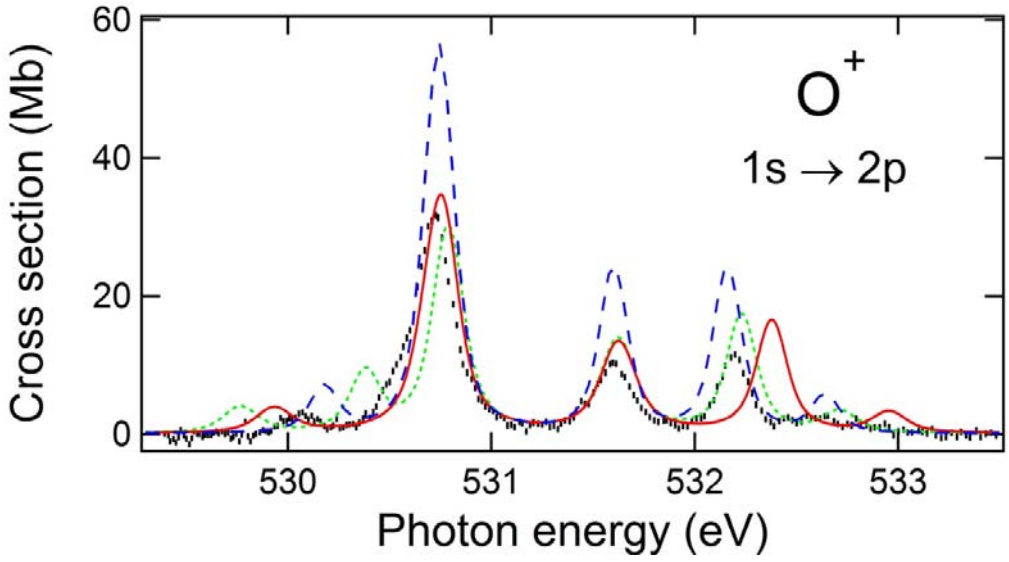

Figure 2: (color on line) Comparison in the region of the 1s → 2p transitions in the O^+ ion of the single photoionization cross section measured with 100 meV BP (black points) with the results of our MCDF (blue dashed line) and *R*-matrix (red continuous line) calculations, as well as with the previous *R*-matrix results of García et al [18] (green dotted line). The theoretical cross sections were reconstructed assuming relative populations of 40% ^{4}S°, 40% ^{2}D° and 20% ^{2}P°, then convolved with a 100 meV FWHM Gaussian profile. The MCDF cross section calculation has been shifted by 1 eV towards higher energies.

$$O^+\ 1s^2\ 2s^2\ 2p^3\ {}^4S^\circ + h\nu \rightarrow O^+\ 1s\ 2s^2\ 2p^4\ {}^4P$$

giving rise to the most intense line number 3. Five additional lines are observed due to the presence in the interaction region of O^+ ions, produced inside the ECRIS source, in the $1s^2\ 2s^2\ 2p^3\ {}^2D^\circ$ and $^2P^\circ$ metastable terms. The O^+ ions produced in highly excited states with a hole in the 1s subshell, due to photon interactions in the beam overlap region, will decay via fast autoionization to the ground terms $1s^2\ 2s^2\ 2p^2\ {}^3P, {}^1D, {}^1S$ of the O^{2+} ion before reaching the detector. The double ionization channel can only be populated by simultaneous ejection of two electrons (shake off) or via three-electron transitions. From the ratio of the integrated intensities of the spectra in the lower and upper panels, we determine that the decay via double ionization channels corresponds to ~ 7% of the decay via single ionization channels.

Figure 2 compares the cross section measured with a 100 meV BP with the results of our MCDF (blue dashed line) and *R*-matrix (red continuous line) calculations, as well as with the previous *R*-matrix results of García et al [18] (green dotted line). The calculated cross sections for the various initial states are weighted to give the best overall agreement with the measured

cross section, favoring the calculated cross section for the ions in the ground state which is expected to be more accurate. In Fig. 2, the relative populations are 40% ^{4}S°, 40% ^{2}D° and 20% ^{2}P° for all reconstructed theoretical cross sections. For an easier comparison with experiment, the calculated cross sections were convolved with a Gaussian profile of 100 meV full width at half maximum (FWHM) to simulate the experimental broadening. The MCDF cross section has been shifted by +1.0 eV on Fig. 2. The measured energies, widths and oscillator strengths of the six lines are given in Table 2. They were obtained by fitting the experimental cross section by six Voigt profiles with equal Gaussian contribution. The numbers in the first column refer to the numbering of the lines used in the middle panel of Fig.1. The assignment of the $1s^2 2s^2 2p^3\ ^{2S_i+1}L_i \rightarrow 1s 2s^2 2p^4\ ^{2S_f+1}L_f$ transitions (2nd column) is obtained from our *R*-matrix and MCDF calculations, where S_i, L_i and S_f, L_f are the spin and the angular momenta of the initial and final states, respectively. The energy of the lines are given in the 3rd column. The numbers in parenthesis give the uncertainties in meV relative to the position of line 3. According to the calibration procedure described previously, the absolute uncertainty is obtained by adding 180 meV to the statistical uncertainty. Our energy value for the line arising from the ion in the ^{4}S ground term (line 3) is compared to the previous measurements of Kawatsura and co-workers [23] using also the merged-beam technique, and to the observations of Chandra [1,2,5,24] and XMM-Newton [3] X-ray satellites (4th column). The final column compares our measured natural widths and oscillator strengths *f* with the results of our MCDF and *R*-matrix calculations, as well as with the results of previous theoretical works [16-18]. The quoted experimental oscillator strengths were obtained from the areas of the lines according:

$$f = 0.0091075 \int \sigma(\hbar\nu)\, d\hbar\nu$$

The values of *f* indicated in Table 2 have been corrected for the initial populations and therefore correspond to transitions for the O^+ ion in the pure ^{4}S°, ^{2}P° or ^{2}D° respective initial states.

The energy we determine for the 1s → 2p transition from the ^{4}S° ground term (530.72 ± 0.18 eV, line 3) is systematically lower than the values extracted from the Chandra and XMM-Newton X-ray observatory spectra, but are in agreement within the respective quoted uncertainties. The highest accuracy determination by Liao and co-workers [5] (530.97 ± 0.03 eV), obtained by selecting 36 high statistics Chandra observations of low-mass X-ray binaries

Table 2: Energies, natural widths and oscillator strengths of the O^+ 1s → 2p lines. Our experimental values are compared to previous measurements and to the results of our MCDF and *R*-matrix calculations, as well as the results of previous theoretical works. The numbers in parenthesis for the experimental determinations of the energies and widths are the estimated uncertainties in meV. For the oscillator strengths, they give the uncertainty in the last figure.

Line	Transition $^{2S_i+1}L_i \rightarrow {}^{2S_f+1}L_f$	Energy (eV)				Width (meV)		Oscillator strength	
		Exp.		Theory		Exp.	Theory	Exp.	Theory
		Merged beam[a]	Satellites	*R*-matrix	MCDF	This work	*R*-matrix	This work	
1	^{2}P° - ^{2}D	530.054(28)		529.936[g]	529.179[l]	86(60)	159[g]	0.039(6)	0.049[g]
				529.768[h]	529.93[b]		162[h]		0.050[h]
				531.096[j]			134.0[j]		0.048[j]
									0.056[l]
2	^{2}P° - ^{2}P	530.522(28)		530.687[g]	529.738[l]		125[g]	0.036(5)	0.093[g]
				530.381[h]	530.24[b]		120[h]		0.097[h]
				531.441[j]			102.6[j]		0.088[j]
									0.124[l]
3	^{4}S° - ^{4}P	530.720	530.96(70)[c]	530.764[g]	529.746[l]	158(20)	134[g]	0.216(32)	0.172[g]
		531.0(500)[b]	531.03(100)[d]	530.789[h]	531.64[b]		129[h]	0.192[d]	0.177[h]
			530.97(30)[e]	533.132[i]			111.6[j]		0.184[i]
			530.80 (50)[f]	532.093[j]					0.167[j]
			530.9(300)[k]						0.244[l]
4	^{2}D° - ^{2}D	531.597(23)		531.627[g]	530.602[l]	159(30)	163[g]	0.063(9)	0.088[g]
				531.623[h]	532.31[b]		160[h]		0.091[h]
				532.841[j]			134.0[j]		0.086[j]
									0.123[l]
5	^{2}D° - ^{2}P	532.190(23)		532.378[g]	531.162[l]	107(20)	126[g]	0.044(7)	0.094[g]
				532.230[h]	532.62[b]		121[h]		0.095[h]
				533.185[j]			102.6[j]		0.088[j]
									0.126[l]
6	^{2}P° - ^{2}S	532.641(44)		532.956[g]	531.641[l]	430(200)	154[g]	0.067(10)	0.040[g]
				532.712[h]	534.05[b]		151[h]		0.040[h]
				533.956[j]			128.2[j]		0.038[j]
									0.056[l]

[a] This work, uncertainty in meV relative to line 3. For absolute uncertainty, add 180 meV.

[b] from ref [23].

[c] from ref [1], Chandra observation.

[d] from ref [2], Chandra observation.

[e] from ref [5], Chandra observation.

[f] from ref [24], Chandra observation.

[g] This work, RMPS.

[h] from ref [18]

[i] from ref [16]
[j] from ref [17].
[K] from ref [3], XMM-Newton observation.
[l] This work, MCDF

and correcting for the shift induced by the Galactic rotation, is however slightly outside. Compared to the theoretical predictions, our determination for the energy of this transition is

systematically lower, by up to 2.4 eV for the relativistic BPRM calculations of Pradhan and co-workers [16]. However, as can be seen in Fig. 2, our RMPS and the BPRM calculations of García et al [18] give results in very good agreement with our measurements. An even more drastic test of the theoretical predictions can be achieved in terms of the relative positions of the lines, which are determined experimentally with higher accuracy than their absolute energies. The two *R*-matrix results shown in Fig. 2 reproduce correctly the relative energy to line 3 only for the $^2D^\circ$ - ^2D transition (line 4). For the low energy part of the spectrum (lines 1 and 2), our calculations give the closest agreement, while those of García et al reproduce better the high energy part (lines 5 and 6). Our MCDF calculations place all the lines 1 eV too low but reproduce very well their relative positions.

The experimental determination of the widths is strongly dependent on the monochromator BP, which is determined through the fitting procedure as the width of the Gaussian contribution to the Voigt profiles. The BP determination was independently verified by measuring the width of the Xe $5p^{-1}$ photoline using the Scienta electron spectrometer, after correction for Doppler and Scienta broadenings. For the natural widths given in Table 2, we fixed for all lines the Gaussian width to the value determined with the Scienta (BP = 100 ± 5 meV). Our measurements of the natural widths of the lines, linked to the lifetimes of the intermediate excited states via the Heisenberg uncertainty principle, are in overall good agreement with the results of the various *R*-matrix calculations, which also agree among themselves. The most pronounced difference is for the ^2P - ^2S transition (line 6) with a measured width three times greater than the calculated widths. In our MCDF calculations, each electric dipole transition was dressed with the same Lorenztian profile with a FWHM given by the autoionization width of the upper level, calculated here to be of the order of 100 meV.

The various *R*-matrix methods give oscillator strengths in close agreement, while our MCDF code predicts higher values. Comparison with the experimental values is not straightforward as the determination of the population of the ions in the different initial states

is model dependent. The uncertainties given in Table 2 for the experimental oscillator strengths

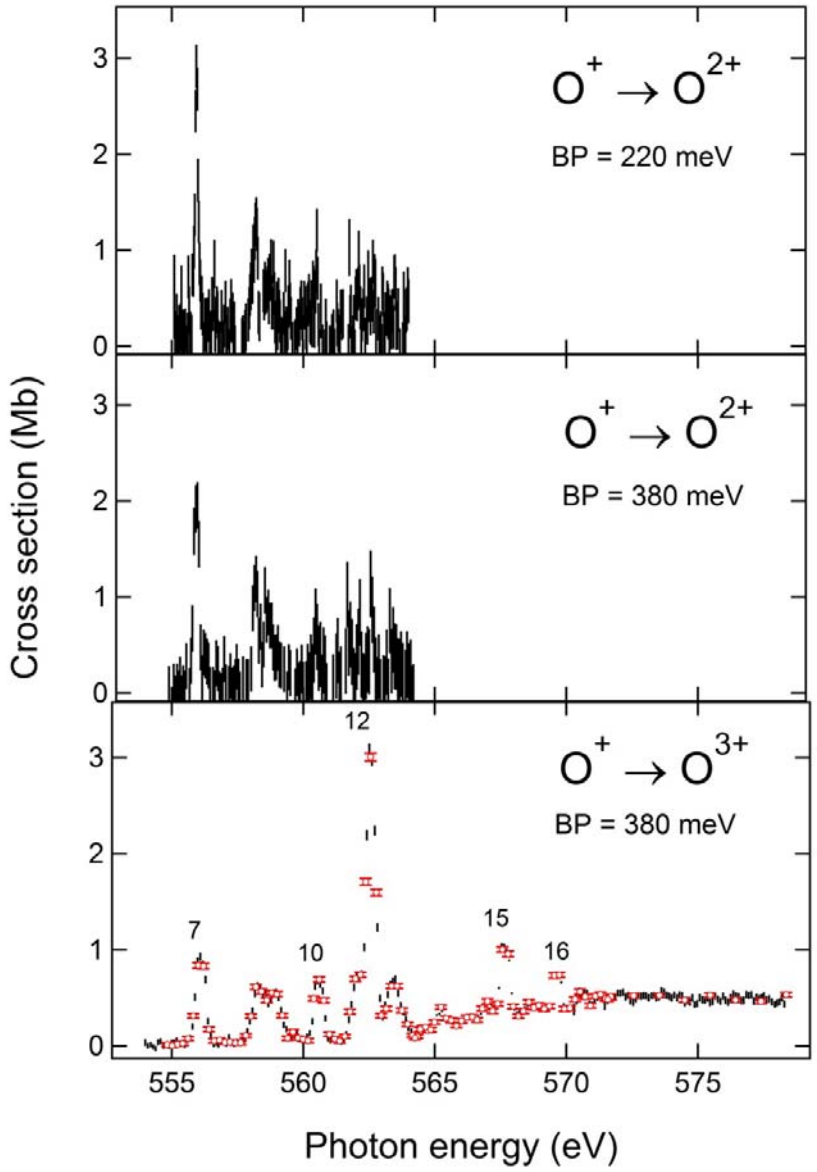

Figure 3. (color on line) Photoionization cross sections measured in the region of the K edges. Upper panel: Single photoionization cross section recorded in the absolute mode with 220 meV BP; Middle panel: Single photoionization cross section recorded in the relative mode with 380 meV BP; Lower panel: Double photoionization cross section recorded in the relative (black points) and absolute (red open circles) modes with 380 meV BP. On all figures, the vertical bars indicate the statistical uncertainties.

do not include any uncertainty in the determination of the populations. Nevertheless, some conclusions can be drawn for transitions from the same initial state. Some strong differences are observed for the photoexcitations starting from the ^{2}P° term, with experimental relative intensities equal to 1/1/2 for the ratios line 1/line 2/line 6 respectively, compared to 1/2/1 for the *R*-matrix and MCDF values. For the ^{4}S° - ^{4}P main line, our measurement is in agreement with the determination from the Chandra spectra by Yao and co-workers [2] as well as with our MCDF result, but is significantly higher than all the *R*-matrix predictions.

Higher 1s → np (n>2) photoexcitations are shown in Fig. 3. The two upper panels exhibit the single photoionization cross section recorded with different BP values, the top one in the absolute mode and the middle one in the relative mode. The bottom panel gives the double photoionization cross sections recorded in relative (black bars) and absolute modes (red open points) with a broader step. For all cross sections, the lengths of the vertical bars indicate the statistical uncertainties for the measurements. The spectra show the transfer of intensity from the single ionization channels to the double ionization channels as the $1s^{-1}$ edge (around 565 eV) is approached. It results from the increasing number of O^{2+} excited intermediate states, offering more decay channels for two step autoionization processes of the type:

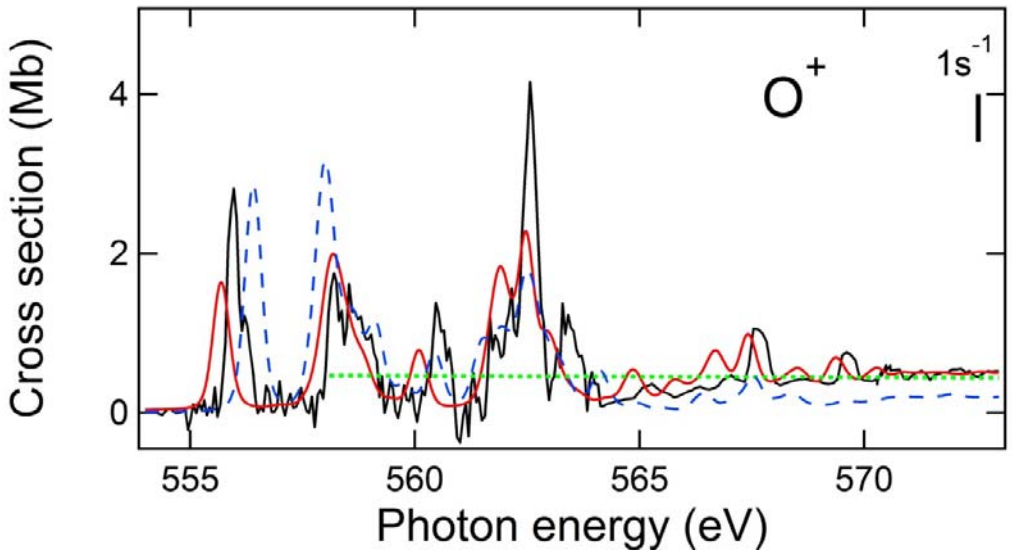

Figure 4. (color on line) Comparison in the region of the 1s → np (n>2) transitions in the O^+ ion of the sum of the measured single and double photoionization cross sections (black line) with the results of our MCDF (blue dashed line) calculations and the previous *R*-matrix results of García et al [18] (red continuous line), reconstructed assuming relative populations of 40% ^{4}S°, 40% ^{2}D° and 20% ^{2}P° and after convolution with a 380 meV FWHM Gaussian profile. The green dotted curve represents the

results of the Hartree-Dirac-Slater calculations of Verner et al [11]. The MCDF cross section has been shifted by 2.5 eV towards higher energies.

Table 3: Energy and oscillator strength of the O^+ 1s → np (n>2) lines. Our experimental values are compared to previous measurements and to the results of our MCDF and previous BPRM work.

Line	Transition	Energy (eV)				Oscillator strength	
		Exp.		Theory		Exp.	Theory
		This work[a]	Satellites[b]	*R*-matrix[d]	MCDF[c]	This work	
7	$^4S°$ →(^5S)3p ^4P	555.93(5)	556.48(8)	555.692	553.928	0.027(4)	0.020[d] 0.031[c]
8	$^2D°$ → 3p	558.12(6)		558.149	555.559		
9	$^2P°$ → 3p	558.75 (6)		558.486	556.156		
10	$^4S°$ → (^5S)4p ^4P	560.42(5)		560.091	557.961	0.014(2)	0.008[d] 0.009[c]
11	$^2D°$, $^2P°$ → 4p	561.85(6)					
12	$^4S°$ → (^3D)3p ^4P	562.40(5)	560.99(13)	562.477	559.991	0.038(6)	0.022[d] 0.016[c]
13	$^2D°$, $^2P°$ → 5p	563.28(6)					
14	$^2D°$, $^2P°$ → 6p	565.26(6)					
15	$^4S°$ → (^3P) 3p ^4P	567.49 (5)		567.422	565.039		
16	$^4S°$ → (^3P) 4p ^4P	569.48(5)		569.342	567.080		

[a] This work, uncertainty in unit of 10 meV relative to line 3. For absolute uncertainty, add 180 meV.

[b] from ref [24], uncertainty in unit of 10 meV .

[c] This work, MCDF.

[d] from ref [18] for the transition from the ground state, private communication for the ones from the metastable states.

$$O^+ \, 1s^2 \, 2s^2 \, 2p^3 + h\nu \rightarrow O^+ \, 1s \, 2s^2 \, 2p^3 \, np \rightarrow O^{2+} \, 1s^2 \, 2s \, 2p^2 \, np + e^-$$

$$O^{2+} \, 1s^2 \, 2s \, 2p^2 \, np \; (n>4) \rightarrow O^{3+} \, 1s^2 \, 2s^2 \, 2p + e^-$$

Above the K edge, the single photoionization cross section is too weak to be measured here (mostly L shell direct photoionization contributes, with a cross section ≈ 0.77 kb according to Verner et al [11]), and the double ionization channel is dominated by direct K shell photoionization followed by Auger decay of the $1s^{-1}$ hole.

To compare the experimental and theoretical cross sections, the contributions of the single and double ionization channels must be added (middle and bottom panels of Fig. 3).

The result is shown in Fig. 4 together with the results of our MCDF calculations, the BPRM calculations of García et al [18] and the Hartree-Dirac-Slater (HDS) single electron calculations of Verner and Yakovlev [11]. The theoretical cross sections were reconstructed assuming again 40% ^{4}S°, 40% ^{2}D° and 20% ^{2}P° initial populations and after convolution with a 380 meV FWHM Gaussian profile to simulate the experimental broadening. The MCDF cross section has been shifted by +2.5 eV in Fig. 4. Once corrected for energy shifts, both the BPRM and MCDF calculated cross sections reproduce the behavior of the experimental cross section over the whole energy range. The MCDF cross section is too low by almost a factor of 2 above 565 eV photon energy, partly because it doesn't include the contribution of the higher members of the 1s → np (n>5) Rydberg series. The HDS calculations place the energy of the $1s^{-1}$ threshold several eV too low (558.1 eV), but reproduce very well the intensity of the direct photoionization cross section, despite the fact that they were performed for the O^+ ion in the ^{4}S ground term only. This demonstrates the low sensitivity of the 1s direct photoionization cross section to the coupling of the initial configuration.

The energies and oscillator strengths of the most intense lines are given in Table 3. The numbers of the lines (1st column) refers to Fig. 3 (bottom panel). Despite the increased complexity of the spectrum due to the presence of O^+ ions in metastable states, tentative assignments of the lines are given in column 2, with the help of the K shell photoabsorption spectrum of atomic nitrogen and BPRM and MCDF calculations [54,18]. Starting from the ^{4}S ground term, 1s → np photoexcitation leads to four Rydberg series 1s $2s^2$ $2p^3$ [^{5}S°,^{3}D°,^{3}S°,^{3}P°] np converging to four $1s^{-1}$ ionization limits. Due to limited spectral resolution, only the highest [^{3}P°] np series can be identified in Fig. 4, leading to the [^{3}P°] K edge around 572.5 eV following Rydberg analysis of the observed lines. The energies of the lines are given in the 3rd column, with the uncertainties relative to line 3 in units of 10 meV (for the total uncertainties, add 180 meV). For these weak transitions, agreement with the energies deduced from Chandra observations (column 4) [24] is much less satisfactory. Assuming that the two lines identified by Gatuzz *et al* as O^+ transitions correspond to the most intense lines we observe (lines 7 and 12), a discrepancy of 2 eV is obtained for the energy separation of the lines. The MCDF calculations place the lines 2.5 eV too low in energy, except line 7 which is shifted by only 2 eV. In contrast, our measurements are in general agreement with the energies calculated by García et al [18], with a global shift of 0.3 eV towards lower energy. The most striking difference with the theoretical predictions is in the intensities of the lines 12 and 13, strongly underestimated by the calculations. The limited BP used in this energy range did not allow for an accurate determination of the natural width of the lines.

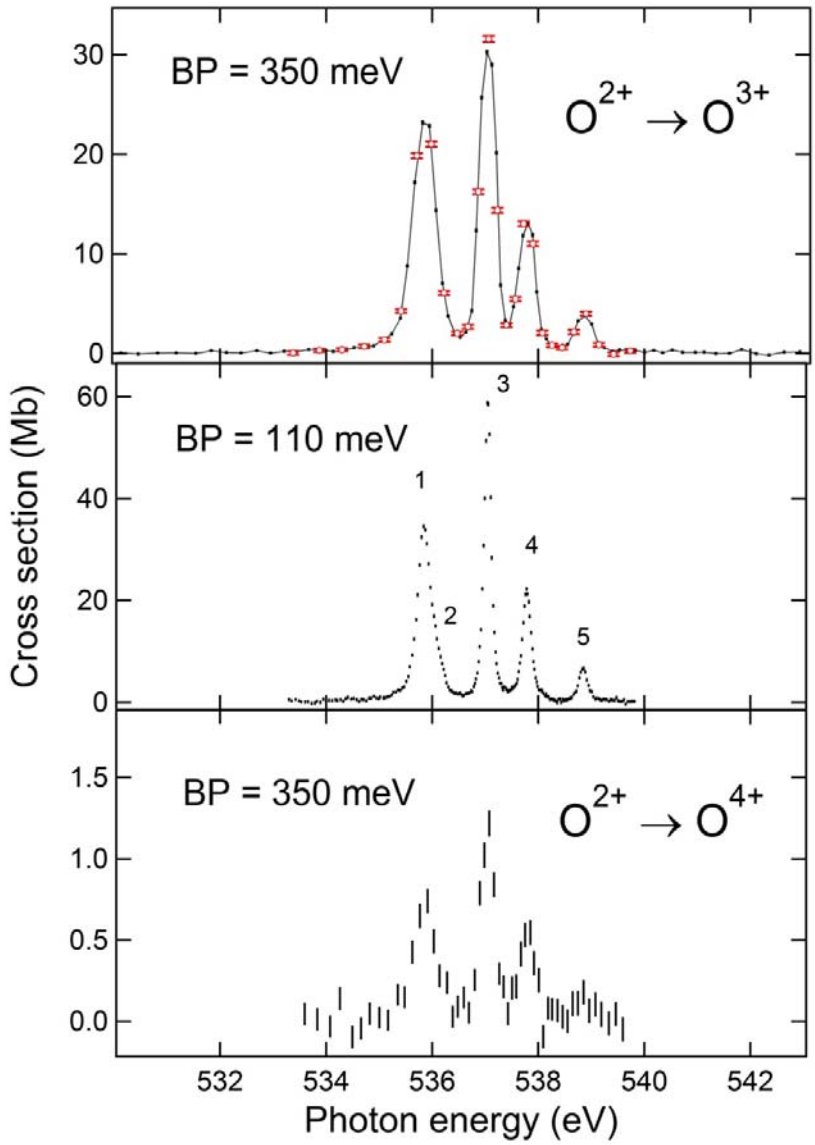

Figure 5. (color on line) Upper panel: Single photoionization cross section recorded in the relative (black points) and absolute modes (red open circles) with 350 meV BP; Middle panel: Single photoionization cross section recorded in the relative mode with 110 meV BP; Lower panel: Double photoionization cross section recorded in the absolute mode with 350 meV BP. On all figures, the vertical bars indicate the statistical uncertainties.

4.2 C-like O^{2+} ion

Figure 5 displays the variation of the single and double photoionization cross sections in the energy range of the 1s → 2p transitions for the O^{2+} ion. Single ionization was recorded with a 350 meV BP (top panel) both in the relative (black points) and absolute (red open circles) modes, and with a 110 meV BP (middle panel) in the relative mode. Double ionization was recorded in the absolute mode with a 350 meV BP (bottom panel). The vertical bars again indicate the statistical uncertainties for all spectra. 1s → 2p photoexcitations from the ground term $1s^2 2s^2 2p^2\ ^3P$ of O^{2+} ion give rise to three lines:

$$O^{2+}\ 1s^2\ 2s^2\ 2p^2\ ^3P + h\nu \rightarrow O^{2+}\ 1s\ 2s^2\ 2p^3\ ^3S°,^3P°,^3D°$$

The highly excited O^{2+} states with one hole in the 1s subshell decay mainly via autoionization to the ground state of the O^{3+} ion:

$$O^{2+}\ 1s\ 2s^2\ 2p^3\ ^3S°,^3P°,^3D° \rightarrow O^{3+}\ 1s^2\ 2s^2\ 2p\ ^2P + e^-$$

Two-electron decays, leading to the ground state of the O^{4+} ion, contribute only 3.2%, a

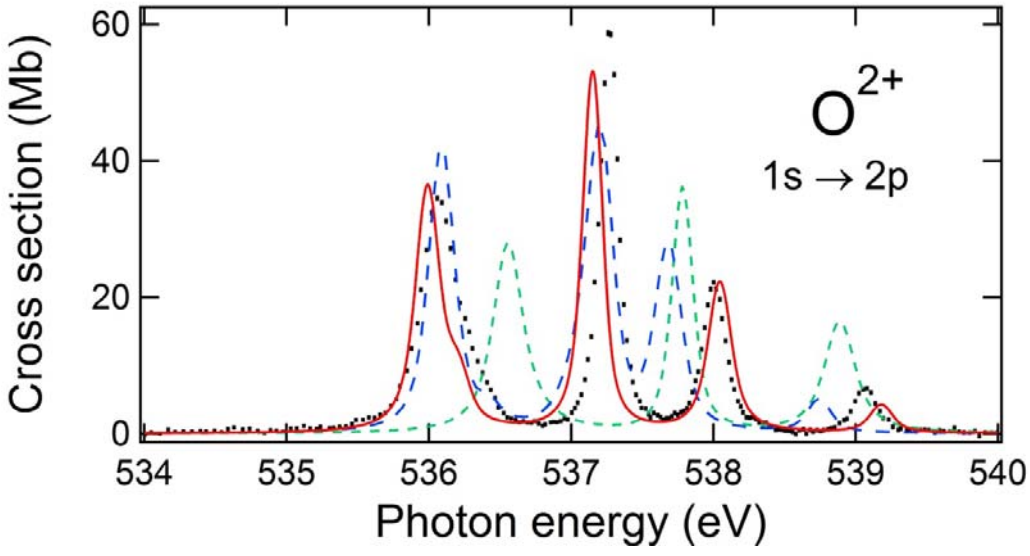

Figure 6. (color on line) Comparison in the region of the 1s → 2p transitions in O^{2+} ion of the single photoionization cross section (black points) measured with 110 meV BP with the results of our MCDF

(blue dashed line) and *R*-matrix (red continuous line) calculations, as well as with the previous *R*-matrix results of García et al [18] (green dotted line), assuming relative populations of 80% ^{3}P, 14% ^{1}D, 4% ^{1}S and 2% ^{5}S°. The theoretical cross sections have been convolved by a 110 meV FWHM Gaussian profile.

factor of two less than in the case of the 1s → 2p transition in O^+ ion but similar to the case of the B-like C^+ ion [48]. The production in the ECRIS of O^{2+} ions in the $1s^22s^22p^2$ ^{1}D,^{1}S and $1s^22s2p^3$ ^{5}S° metastable states is responsible for the additional lines observed on the spectra. The comparison of the measurements done at 110 meV BP with our theoretical RMPS and MCDF calculations is displayed on Fig. 6, together with the BPRM results of García et al [18]. The theoretical cross sections were reconstructed assuming the population of the ions in the different initial states to be the same as determined by Champeaux et al [55] (80% ^{3}P, 14% ^{1}D, 4% ^{1}S, 2% ^{5}S°). In their work an ECRIS source was also used to study the valence photoionization of the O^{2+} ion, and the populations were determined from the height at threshold of the onsets of the direct photoionization cross sections observed on the experimental spectrum, normalized to their MCDF calculated cross sections. These calculations show the small dependence of the cross sections on the coupling of the $1s^22s^22p^2$ initial configuration. Since García et al [18] calculated the cross section for the ^{3}P ground state only, their results have been multiplied by 0.8 for a better comparison with the other results. All the theoretical cross sections have been convolved with a 110 meV FWHM Gaussian profile to simulate the experimental broadening. The measured energies, widths and oscillator strengths for the various lines are reported in Table 4. They are compared to the results of our RMPS and MCDF calculations, as well as with the predictions of previous calculations. The numbering of the lines (column 1) refers to the experimental spectrum shown in the middle panel of Fig. 5. The assignments of the $1s^22s^22p^2, 1s^22s2p^{3\ 2S_i+1}L_i \rightarrow 1s2s^22p^{3\ 2S_f+1}L_f$ transitions (2nd column) are obtained from our calculations. Of the seven lines predicted theoretically, only five are observed. For both calculations, the ^{1}D → ^{1}D° line is not resolved from the ^{3}P → ^{3}S° line (line 3). Line 2 is assigned by the *R*-matrix calculations as due to the unresolved ^{5}S° → ^{5}P and ^{1}S → ^{1}P resonances while the MCDF calculations place the ^{5}S° → ^{5}P transition at the same energy as line 3. The numbers in parenthesis given after the measured positions of the lines (column 3) are the uncertainties in meV relative to the position of line 3. The total uncertainties are again obtained by adding 180 meV. The measured position of line 3 is in agreement with the previous EBIT measurement of Gu et al [22]. Nevertheless, it is distinctly lower by at least

0.5 eV when compared to the energies deduced from Chandra and XMM Newton observations [24] [3] [5]. For the lines arising from the ^{3}P ground term (lines 1, 3 and 4), the three calculations shown in Fig. 6 reproduce quite well the general behavior of the experimental spectra, the best agreement being achieved by our RMPS calculations. We note also in Table 4

Table 4: Energies, widths and oscillator strengths of the O^{2+} 1s → 2p lines. Our experimental values are compared to previous measurements and to the results of our MCDF and *R*-matrix calculations, as well as the results of previous theoretical works. The numbers in parenthesis for all the experimental determinations of the energies and widths are the estimated uncertainties in meV. For the oscillator strengths, they give the uncertainty of the last figure.

Line	Transition	Energy (eV)				Width (meV)		Oscillator strength		
		Exp.		Theory		Exp.	Theory	Exp.	Theory	
		Lab.	Satellites	*R*-matrix	MCDF	This work		This work	*R*-matrix	MCDF
1	^{3}P - ^{3}D°	536.082(23)[a]	536.635(116)[c]	535.992[a]	536.090[a]	135(8)	146[a]	0.098(15)	0.117[a]	0.137[a]
				540[f]	531.836[k]		132[f]		0.119[g]	
				537.2[g]			128[h]		0.111[j]	
				537.976[h]			143[i]			
				535.286[i]			207[j]			
				536.559[j]			186[k]			
2	^{1}S - ^{1}P°	536.254(29)[a]		536.190[a]	536.422[a]	163(26)	134[a]		0.291[a]	0.335[a]
				537.947[h]	538.596[k]		112[h]			
							153[k]			
	^{5}S° - ^{5}P			536.235[a]	536.997[a]		72[a]		0.203[a]	0.232[a]
				534[f]	539.315[k]		87[f]			
				538.243[h]			68[h]			
							186[k]			
	^{1}D - ^{1}D°			537.128[a]	537.138[a]		140[a]		0.218[a]	0.251[a]
				543[f]	535.878[k]		118[f]			
				538.924[h]			116[h]			
							153[k]			
3	^{3}P - ^{3}S°	537.269[a]	537.80(20)[c]	537.156[a]	537.220[a]	102(7)	79[a]	0.145(22)	0.097[a]	0.105[a]
		537.408(93)[b]	536(1000)[d]	540[f]	533.664[k]		58[f]		0.102[g]	
			537.95(180)[e]	538.6[g]			56[h]		0.095[j]	
				538.901[h]			61[i]			
				536.496[i]			106[j]			
				537.784[j]			107[k]			

4	^{3}P - ^{3}P°	538.007(22)[a]		538.046[a] 541[f] 540.7[g] 540.195[h] 537.350[i] 538.888[j]	537.681[a] 533.970[k]	174(6)	139[a] 110[f] 128[h] 137[i] 213[j] 186[k]	0.078(12)	0.070[a] 0.067[g] 0.080[j]	0.092[a]
5	^{1}D - ^{1}P°	539.068(4)[a]		539.181[a] 545[f] 541.138[h]	538.744[a] 537.979[k]	102(17)	134[a] 111[f] 110[h] 153[k]	0.093(14)	0.072[a]	0.087[a]

[a] This work. Uncertainty on the experimental values in meV relative to line 3. For absolute uncertainty, add 180 meV.

[b] EBIT [22]

[c] from [24], Chandra observation

[d] from [3], XMM Newton observation

[e] from [5], Chandra observation

[f] *R*-matrix from [13]

[g] *R*-matrix from [16]

[h] *R*-matrix from [14]

[i] *R*-matrix from [15]

[j] *R*-matrix from [18]

[k] MCDF from [12]

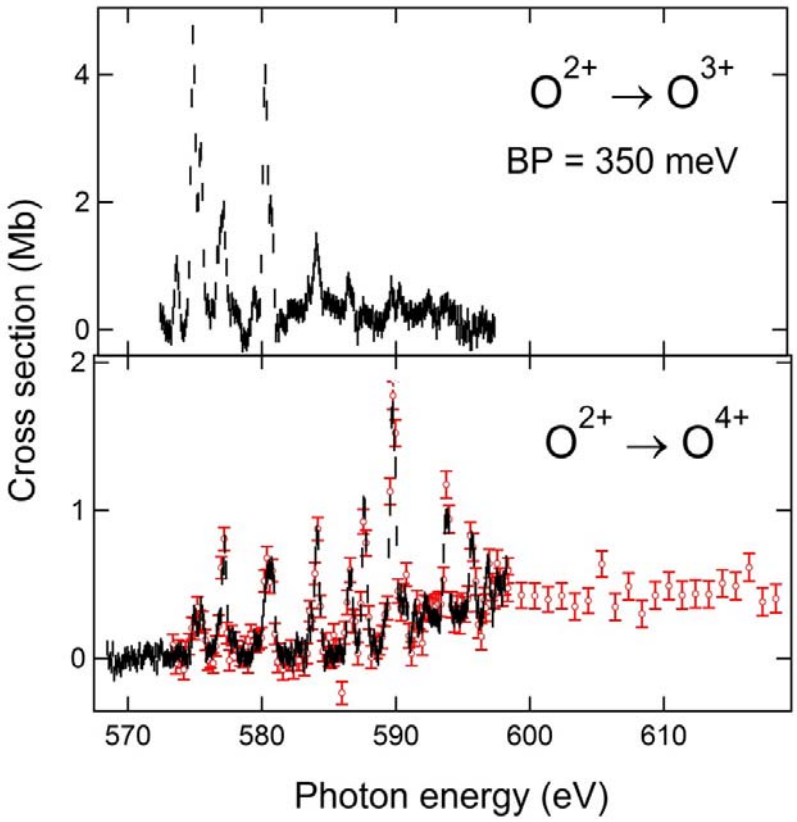

Figure 7. (color on line) Photoionization cross sections measured in the region of the K edges for O^{2+} ion. Upper panel: Single photoionization cross section recorded in the absolute mode with 350 meV BP; Lower panel: Double photoionization cross section recorded in the relative (vertical bars) and absolute (red open circles) modes with 350 meV BP. On all figures, the vertical bars indicate the statistical uncertainties.

the strong dispersion of the various theoretical energies which are globally higher than the experimental values, except for our RMPS determinations which reproduce fairly well the spacing of the lines. The same observations can be made for line 5 arising from the ^1D initial term. The measured widths of the lines are in general higher than the width determined by the RMPS method. In our MCDF calculations the widths were estimated by calculating the autoionization rate for the $1s^2\ 2s^2\ 2p^2$ mean configuration (131 meV). The same natural width was used to dress all the lines of the MCDF cross section shown in Fig. 6. Direct comparison of the measured and theoretical oscillator strengths can be made only for lines 4 and 5 which are pure. The agreement for these lines is good for all models. As for Tables 2 and 3, the oscillator strengths given in Table 4 were corrected for the populations of the initial states. Although a 10% accuracy can reasonably be expected on the calculated direct photoionization

cross sections used to estimate the populations, we preferred once again not to include its contribution to the accuracy on the oscillator strengths given in Tables 4 and 5, considering the values given by Champeaux et al were obtained with an ECR ion source slightly different from ours.

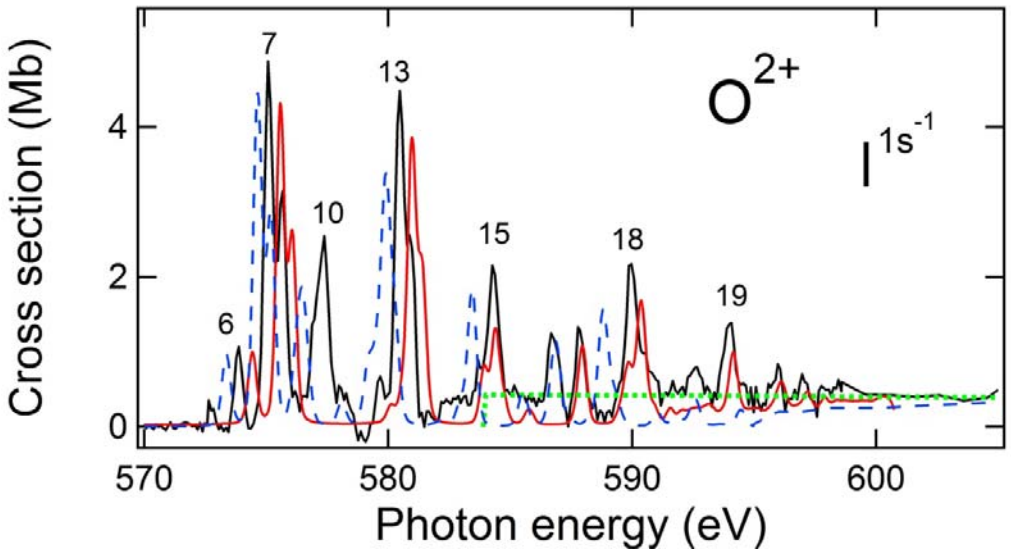

Figure 8. (color on line) Comparison in the region of the 1s → np (n>2) transitions in O^{2+} ion of the sum of the measured single and double photoionization cross sections (black line) with the results of our MCDF (blue dashed line) calculations, as well as with the previous *R*-matrix results of García et al [18] (red continuous line), assuming relative populations of 80% ^{3}P, 14% ^{1}D, 4% ^{1}S and 2% ^{5}S. The green dotted curve represents the Hartree-Dirac-Slater calculations of Verner et al [11].

The higher 1s → nl (n>2) photoexcitations are shown in Fig. 7. The top panel displays the variation of the single photoionization cross section recorded in the absolute mode, and the bottom panel shows the variation of the double photoionization cross section recorded in the relative (black points) and absolute (red open circles) modes. The lengths of the vertical bars for each point indicate the statistical uncertainties. As for the O^+ ion, we note the vanishing intensity of the single ionization channels on approaching the $1s^{-1}$ ionization thresholds (around 595 eV), while the intensity of the double ionization channels increases to reach a constant value, above the thresholds representing direct 1s photoionization followed by the Auger decay of the $1s^{-1}$ hole. Figure 8 compares the sum of the experimental single and double photoionization cross section with the results of our MCDF calculations (blue dashed curve), reconstructed by assuming an 80% ^{3}P, 14% ^{1}D, 4% ^{1}S and 2% ^{5}S° population of the initial term and after convolution with a 350 meV FWHM Gaussian profile. The results of the

previous BPRM calculations by García et al [18] for the ^{3}P ground term are also shown as the continuous red line. They have been multiplied by 0.8 to take into account the 80% population of the ^{3}P term in the experimental spectrum, and then convolved with the Gaussian profile. The positions and oscillator strengths of the observed lines are summarized in Table 5. The numbering of the lines (1st column) refers to Fig. 8. The assignments (2nd column) are obtained from our MCDF calculations. The uncertainties relative to line 3 for the measured positions of the lines (3rd column) are indicated by the numbers in parenthesis in units of 10 meV. As previously, 180 meV must be added to get the absolute uncertainties. The energies obtained by the MCDF and BPRM methods are given in columns 4 and 5, respectively. The last columns compare the measured and calculated oscillator strengths when corrected for the population of the initial state. The numbers in parenthesis give the uncertainty for the last figure, without contribution of the uncertainty for the initial state population. Our MCDF results reproduce very well the general behavior and the intensity of the lines of the measured cross section, but show a shift towards lower energy, increasing continuously from 0.5 eV at the position of line 6, to 1.5 eV for line 20. The BPRM results show also good agreement for the lines arising from the ^{3}P ground term, but with a shift in energy toward higher values, decreasing from 0.5 eV at line 6 to 0.2 eV at line 20. Starting from the ^{3}P ground term, three Rydberg series 1s 2s^2 2p^3[^{2,4}P]np ^{3}S°,^{3}P°,^{3}D° are expected, converging to the two ^{2,4}P thresholds. Due to the moderate resolution used in this energy range, only one series can be identified up to n = 7 on the experimental spectrum, converging to a threshold around 599.6 eV. The 1s direct photoionization cross section calculated for ions in the ^{3}P ground term by the HDS method [11] is also shown in Fig. 8 (green dotted line). The three theoretical cross sections reproduce very well the intensity of

Table 5: Energy and oscillator strength of the O^{2+} 1s → np (n>2) lines. Our experimental values are compared to the results of our MCDF calculations and of the previous BPRM work of García and coll. [18].

Line	Transition	Energy (eV)			Oscillator strength		
		Exp.	Theory		Exp.	Theory	
		This work[a]	R-matrix[b]	MCDF[a]	This work	R-matrix[d]	MCDF[a]
6	^{3}P→3p^{3}S	573.86(14)	574.43	573.36	0.0046(7)	0.0059	0.0055
7	^{3}P→3p^{3}D	575.09(14)	575.57	574.65	0.025(4)	0.021	0.023
8	^{3}P→3p^{3}P	575.65(14)	576.07	575.18	0.016(3)	0.013	0.015
9	^{1}D→3p^{1}D	577.05(37)		576.18	0.086(13)		0.019

10	$^1D \rightarrow 3p^1F$	577.38(23)		576.45	0.047(7)		0.040
11	$^1D \rightarrow 3p^1P$	578.19(22)		576.68	0.016(2)		0.012
12	$^3P \rightarrow$	579.65(16)	580.11		0.0024(4)	0.0029	
13	$^3P \rightarrow 3p^3D$	580.47(14)	580.97	579.90	0.026(4)	0.021	0.016
14	$^3P \rightarrow 3p^3P$	580.95(15)	581.39	580.27	0.010(2)	0.011	0.0073
15	$^3P \rightarrow 4p^3D$	584.33(12)	584.39	583.44		0.0078	0.012
16	$^1D \rightarrow 4p^1F$	586.81(15)		585.50			0.015
17	$^3P \rightarrow 4p^3P$	587.88(14)	587.94	586.83		0.0062	0.0069
18	$^3P \rightarrow 4p^3D$	590.01(3)	590.31	588.76		0.0092	0.010
19	$^3P \rightarrow 5p^3D$	593.99(14)	594.15	592.51			0.0026
20	$^3P \rightarrow 6p^3D$	595.90(14)	596.10	594.42			0.0014
21	$^3P \rightarrow 7p^3D$	597.08(15)	597.20				

[a] This work, uncertainty in unit of 10 meV relative to line 3. For absolute uncertainty, add 180 meV.

[b] from [18].

this process, showing the relatively low importance of the electron correlation effects not included in the HDS method. The same observation was done already in the case of the direct 1s photoionization cross section along the oxygen iso-nuclear sequence [56]. Removal of 2s or 2p electrons has no effect on the 1s photoionization cross section other than shifting the threshold. As previously observed for the O^+ ion, the HDS method places the 1s threshold too low by several eV.

4.3 Comparison between satellites and SR experiments

Marked discrepancies were recently noted between the energies measured by synchrotron radiation based experiments for neutral oxygen [26] and the O^{3+} ion [9] and X-ray satellite

observations [5,24]. The energies of the 1s → 2p transitions for the first members of the oxygen iso-nuclear series as determined by Chandra observations and SR experiments are summarized in Table 6. For the O^{3+} ion, energies measured at SOLEIL with our merged-beam experiment [9] have been recalibrated using the revised photon energy calibration (see section 2.3) which we believe to be more reliable. While there is good agreement within the respective

Table 6: Comparison of the energy (in eV) of the 1s → 2p lines for the first members of the O iso-nuclear sequence in their ground state determined from the Chandra observations and by the synchrotron radiation (SR) based experiments. The numbers in parenthesis give the absolute uncertainties in meV.

		Gatuzz et al [24]	Liao et al [5]	SR Exp.
O		527.548(22)	527.397(13)	526.790(40)[a]
O^+		530.800(45)	530.966(25)	530.720(180)[b]
O^{2+}	^3D	536.635(116)		536.082(203)[b]
	^3S	537.799(23)	537.942(18)	537.269(180)[b]
	^3P			538.007(202)[b]
O^{3+}	^2D			543.823(213)[c]
	$^2P°$		546.263(79)	545.014(181)[c]
	^2S			547.128(225)[c]

[a] from [26].
[b] this work
[c] from [9] after recalibration (see text).

uncertainties in the case of the O^+ ion, discrepancies previously observed for neutral oxygen and the O^{3+} ion (the Chandra measurements being higher by 0.6 eV and 1.2 eV for neutral O and O^{3+}, respectively) are also present for the O^{2+} ion, our measurements indicating energies 0.5 eV lower than those deduced from the satellite spectra. We have no final explanation up to now for such discrepancies. Our work indicates it is not attributed to a wrong energy calibration in the SR based experiments. Furthermore, in the satellite observations, it is assumed that all the elements are in their gas phase. No account is taken of molecular or solid-state effects (grains) which can lead to as much as 0.5 eV – 1.0 eV shift in the K-line positions. We speculate that this may be the differences between the SR measurements and

the satellite observations. We note also that the spectral resolution of the X-ray observatories (maximum resolving power ≈ 1000 compared to 5300 in the present work) is not sufficient to resolve the three transitions from the ground term in O^{2+} and O^{3+} ions, making more uncertain the identification of the lines in the X-ray satellites spectra.

5. Conclusion

Absolute cross sections for K-shell photoionization of nitrogen-like O^{+} and carbon-like O^{2+} ions were measured by employing the ion-photon merged-beam technique. High-resolution spectroscopy up to $E/\Delta E \approx 5300$ was achieved in the photon energy range 526 eV – 540 eV where the strong $1s \rightarrow 2p$ photoexcitations are observed, and $E/\Delta E \approx 1700$ in the region 553 - 620 eV of the weaker $1s \rightarrow np$ ($n>2$) transitions converging to the 1s ionization thresholds. Rich resonance structures, observed in the experimental spectra, were analyzed and identified with the aid of *R*-matrix and MCDF methods. We characterize the strong $1s \rightarrow 2p$ and the weaker $1s \rightarrow 3p$ resonances observed in the K shell spectra of these two important atomic oxygen ions. To try to understand the discrepancy observed between the measurements of the X-ray observatories and the SR based experiments on the energy of the K_{α} transitions in the O iso-nuclear sequence, special care was taken in the energy calibration of the $1s \rightarrow 2p$ resonances. We observe the determinations by the SR based experiments are systematically lower than those performed by the satellites for neutral oxygen, O^{2+} and O^{3+} ions. These differences are yet unexplained and would require further investigation. One potentially useful course of action could be to recalibrate the satellite data, according to the resonance energies determined in the SR works. This will provide new energies for the remaining resonances in the satellite spectra, which may help in their identification. If this indeed were to be the case, then this would also provide simultaneous confirmation of the revised resonance energies.

A major strength of the present study is the high spectral resolution of the spectra, and associated theoretical predictions made using state-of-the-art MCDF and *R*-matrix with pseudo-states methods. Our theoretical results, obtained for ions in both the ground and metastable states, have been compared with high-resolution experimental measurements and with other theoretical methods. They should be suitable for incorporation into astrophysical modeling codes such as CLOUDY [57,58], XSTAR [20] and AtomDB [59] used to numerically simulate the thermal and ionization structures of ionized astrophysical nebulae.

Acknowledgments

The authors thank the SOLEIL staff and in particular Egill Antonsson of the PLEIADES beam line for helpful assistance during the measurements, and John Bozek and Minna Patanen for their help in the energy calibration of the beam line. M F Gharaibeh acknowledges funding from the Scientific Research Support Fund, Jordan, under contract number Bas/2/02/2010. I Q Ababneh acknowledges financial support from the SESAME – Lounsbery foundation for a training fellowship. B M McLaughlin acknowledges support from the US National Science Foundation through a grant to ITAMP at the Harvard- Smithsonian Center for Astrophysics, the RTRA network Triangle de la Physique and a visiting research fellowship (VRF) from Queen's University Belfast. We thank E T Kennedy for careful reading of the manuscript and constructive comments. J C Raymond and R K Smith at the Harvard-Smithsonian Center for Astrophysics are acknowledge for many helpful discussions on the astrophysical applications. The *R* matrix computational work was carried out at the National Energy Research Scientific Computing Center in Oakland, CA, USA and at the High Performance Computing Center Stuttgart (HLRS) of the University of Stuttgart, Stuttgart, Germany. This research also used resources of the Oak Ridge Leadership Computing Facility at the Oak Ridge National Laboratory, which is supported by the Office of Science of the U.S. Department of Energy under Contract No. DE-AC05-00OR22725.

References

[1] A.M. Juett, N.S. Schultz, and D. Chakrabarty, Astrophys. J. **612**, 308 (2004).
[2] Y. Yao, N. S. Schulz, M. F. Gu, M. A. Nowak, and C. R. Canizares, Astrophys. J. **696**, 1418 (2009).
[3] G. Sala, J. Greiner, E. Bottacini, and F. Haberl, Astrophys. Space Sci. **309**, 315 (2007).
[4] C. Pinto, J. S. Kaastra, E. Costantini, and C. de Vries, Astron. Astrophys. **551**, A25 (2013).
[5] J.-Y. Liao, S.-N. Zhang, and Y. Yao, Astrophys. J. **774**, 116 (2013).
[6] K. C. Steenbrugge, J. S. Kaastra, C. P. de Vries, and R. Edelson, Astron. Astrophys. **402**, 477 (2003).
[7] J. M. Ramírez, Astron. Astrophys. **551**, A95 (2013).
[8] T. Kallman, D. A. Evans, H. Marshall, C. Canizares, A. Longinotti, M. Nowak, and N. Schulz, Astrophys. J. **780**, 121 (2014).
[9] B. M. McLaughlin, J. M. Bizau, D. Cubaynes, M. M. A. Shorman, S. Guilbaud, I. Sakho, C. Blancard, and M. F. Gharaibeh, J. Phys. B At. Mol. Opt. Phys. **47**, 115201 (2014).
[10] R. F. Reilman and S. T. Manson, Astrophys J Suppl Ser **40**, 85 (1979).

[11] D. A. Verner, D. G. Yakovlev, I. M. Band, and M. B. Trzhaskovskaya, At. Data Nucl. Data Tables **55**, 233 (1993).
[12] M. H. Chen, K. J. Reed, D. M. McWilliams, D. S. Guo, L. Barlow, M. Lee, and V. Walker, At. Data Nucl. Data Tables **65**, 289 (1997).
[13] D. Petrini and E. P. da Silva, Rev Mex Astron Astro **32**, 69 (1996).
[14] J. Zeng, J. Yuan, and Q. Lu, J. Phys. B At. Mol. Opt. Phys. **34**, 2823 (2001).
[15] E. Olalla, N. J. Wilson, K. L. Bell, I. Martin, and A. Hibbert, Mon. Not. R. Astron. Soc. **332**, 1005 (2002).
[16] A. K. Pradhan, G. X. Chen, F. Delahaye, S. N. Nahar, and J. Oelgoetz, Mon. Not. R. Astron. Soc. **341**, 1268 (2003).
[17] J. Zeng, G. Zhao, and J. Yuan, Eur. Phys. J. - At. Mol. Opt. Phys. **28**, 163 (2004).
[18] J. García, C. Mendoza, M. A. Bautista, T. W. Gorczyca, T. R. Kallman, and P. Palmeri, Astrophys. J. Suppl. Ser. **158**, 68 (2005).
[19] M. A. Bautista and T. R. Kallman, Astrophys. J. Suppl. Ser. **134**, 139 (2001).
[20] T. Kallman and M. Bautista, Astrophys. J. Suppl. Ser. **133**, 221 (2001).
[21] R. Bruch, D. Schneider, W. H. E. Schwarz, M. Meinhart, B. M. Johnson, and K. Taulbjerg, Phys. Rev. A **19**, 587 (1979).
[22] M. F. Gu, M. Schmidt, P. Beiersdorfer, H. Chen, D. B. Thorn, E. Träbert, E. Behar, and S. M. Kahn, Astrophys. J. **627**, 1066 (2005).
[23] K. Kawatsura, H. Yamaoka, M. Oura, T. Hayaishi, T. Sekioka, A. Agui, A. Yoshigoe, and F. Koike, J. Phys. B At. Mol. Opt. Phys. **35**, 4147 (2002).
[24] E. Gatuzz, J. García, C. Mendoza, T. R. Kallman, M. Witthoeft, A. Lohfink, M. A. Bautista, P. Palmeri, and P. Quinet, Astrophys. J. **768**, 60 (2013).
[25] W. C. Stolte, Y. Lu, J. a. R. Samson, O. Hemmers, D. L. Hansen, S. B. Whitfield, H. Wang, P. Glans, and D. W. Lindle, J. Phys. B At. Mol. Opt. Phys. **30**, 4489 (1997).
[26] B. M. McLaughlin, C. P. Ballance, K. P. Bowen, D. J. Gardenghi, and W. C. Stolte, Astrophys. J. Lett. **771**, L8 (2013).
[27] O. Travnikova, J.-C. Liu, A. Lindblad, C. Nicolas, J. Söderström, V. Kimberg, F. Gel'mukhanov, and C. Miron, Phys. Rev. Lett. **105**, 233001 (2010).
[28] C. Miron, C. Nicolas, and E. Robert, http://www.synchrotronsoleil.fr/Recherche/LignesLumiere/PLEIADES (2014).
[29] M. F. Gharaibeh, D. Cubaynes, S. Guilbaud, N. E. Hassan, M. M. A. Shorman, C. Miron, C. Nicolas, E. Robert, C. Blancard, B. M. McLaughlin, and J. M. Bizau, J. Phys. B At. Mol. Opt. Phys. **44**, 175208 (8pp) (2011).
[30] J. A. R. Samson, in *Techniques of Vacuum Ultraviolet Spectroscopy*, John Wiley & Sons (New-York, 1967), p. 266.
[31] T. Tanaka, R. Feifel, M. Kitajima, H. Tanaka, S. L. Sorensen, R. Sankari, A. De Fanis, M.-N. Piancastelli, L. Karlsson, and K. Ueda, Phys. Rev. A **78**, 022516 (2008).
[32] G. R. Wight and C. E. Brion, J. Electron Spectrosc. Relat. Phenom. **4**, 313 (1974).
[33] A. P. Hitchcock and C. E. Brion, J. Electron Spectrosc. Relat. Phenom. **18**, 1 (1980).
[34] M. Coreno, M. de Simone, K. C. Prince, R. Richter, M. Vondráček, L. Avaldi, and R. Camilloni, Chem. Phys. Lett. **306**, 269 (1999).
[35] R. N. S. Sodhi and C. E. Brion, J. Electron Spectrosc. Relat. Phenom. **34**, 363 (1984).
[36] M. Larsson, P. Baltzer, S. Svensson, B. Wannberg, N. Martensson, A. N. de Brito, N. Correia, M. P. Keane, M. Carlsson-Gothe, and L. Karlsson, J. Phys. B At. Mol. Opt. Phys. **23**, 1175 (1990).
[37] A. Kramida, Y. A. Ralchenko, J. Reader, and NIST ASD Team, NIST At. Spectra Database (ver. 5.2), [Online]. Available: http://physics.nist.gov/asd (2014), National Institute of Standards and Technology, Gaithersburg, MD.
[38] J. D. Wright, T. J. Morgan, L. Li, Q. Gu, J. L. Knee, I. D. Petrov, V. L. Sukhorukov, and H. Hotop, Phys. Rev. A **77**, 062512 (2008).

[39] J. Bruneau, J. Phys. B At. Mol. Phys. **17**, 3009 (1984).
[40] P.G. Burke, in *R-Matrix Theory of Atomic Collision: Application to Atomic, Molecular and Optical Processes* (Springer Berlin Heidelberg, 2011), pp. 379–432.
[41] C. P. Ballance and D. C. Griffin, J. Phys. B At. Mol. Opt. Phys. **39**, 3617 (2006).
[42] B. M. McLaughlin and C. P. Ballance, J. Phys. B At. Mol. Opt. Phys. **45**, 085701 (2012).
[43] B. M. McLaughlin and C. P. Ballance, J. Phys. B At. Mol. Opt. Phys. **45**, 095202 (2012).
[44] E. Clementi and C. Roetti, At. Data Nucl. Data Tables **14**, 177 (1974).
[45] K. Berrington, L. Quigley, and H. L. Zhang, J. Phys. B At. Mol. Opt. Phys. **30**, 5409 (1997).
[46] A. Hibbert, Comput. Phys. Commun. **9**, 141 (1975).
[47] B. M. McLaughlin, and C. P. Ballance, in *Sustained Simulated Performance* 2014, edited by M. Reich, Y. Kovalenko, E. Focht, W. Bez, and H. Kobaysahi (Springer, New York and Berlin, 2014), Chap. 15.
[48] B. M. McLaughlin, C. P. Ballance, M S Pindzola, and A. Muller, in *High Performance Computing in Science and Engineering* 2014, edited by W. E. Nagel, D. B. Kroner, and M. Reich (Springer, New York and Berlin, 2014), Chap. 4.
[49] U. Fano and J. W. Cooper, Rev. Mod. Phys. **40**, 441 (1968).
[50] B. W. Shore, Rev. Mod. Phys. **39**, 439 (1967).
[51] L. Quigley and K. Berrington, J. Phys. B At. Mol. Opt. Phys. **29**, 4529 (1996).
[52] L. Quigley, K. Berrington, and J. Pelan, Comput. Phys. Commun. **114**, 225 (1998).
[53] C. P. Ballance, K. A. Berrington, and B. M. McLaughlin, Phys. Rev. A **60**, R4217 (1999).
[54] M. M. Sant'Anna, A. S. Schlachter, G. Öhrwall, W. C. Stolte, D. W. Lindle, and B. M. McLaughlin, Phys. Rev. Lett. **107**, 033001 (2011).
[55] J. P. Champeaux, J.-M. Bizau, D. Cubaynes, C. Blancard, S. N. Nahar, D. Hitz, J. Bruneau, and F. J. Wuilleumier, Astrophys. J. Suppl. Ser. **148**, 583 (2003).
[56] D.W. Missavage, S.T. Manson and G.R. Daum, Phys. Rev. A **15**, 1001 (1977).
[57] G. J. Ferland, K. T. Korista, D. A. Verner, J. W. Ferguson, J. B. Kingdon, and E. M. Verner, Publ. Astron. Soc. Pac. **110**, 761 (1998).
[58] G. J. Ferland, Annu. Rev. Astron. Astrophys. **41**, 517 (2003).
[59] A. R. Foster, L. Ji, R. K. Smith, and N. S. Brickhouse, Astrophys. J. **756**, 128 (2012).